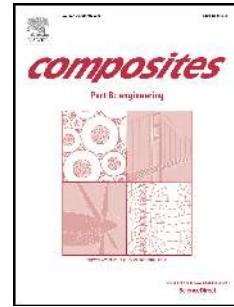# Journal Pre-proof

Enhanced performance of 3D printed highly elastic strain sensors of carbon nanotube/thermoplastic polyurethane nanocomposites via non-covalent interactions

Dong Xiang, Xuezhong Zhang, Yuntao Li, Eileen Harkin-Jones, Yongfeng Zheng, Lei Wang, Chunxia Zhao, Ping Wang

Enhanced performance of 3D printed highly elastic strain sensors of carbon nanotube/thermoplastic polyurethane nanocomposites via non-covalent interactions

Dong Xiang[a,*,#], Xuezhong Zhang[a,#], Yuntao Li[a,*], Eileen Harkin-Jones[b], Yongfeng Zheng[a], Lei Wang[a], Chunxia Zhao[a], Ping Wang[a]

[a]School of Materials Science and Engineering, Southwest Petroleum University, Chengdu 610500, China

[b]School of Engineering, University of Ulster, Jordanstown BT37 0QB, UK

[*]Corresponding authors: dxiang01@hotmail.com (Dong Xiang); yuntaoli@swpu.edu.cn (Yuntao Li)

([#]These authors contributed equally to this work.)

Abstract: Strain sensors based on conductive polymer composites have been widely investigated due to their excellent elasticity and sensitivity. Such sensors may be manufactured using additive manufacturing techniques but there are some challenges to overcome in terms of performance if this technique is to be used. In this work, a high-performance strain sensor of carbon nanotube/thermoplastic polyurethane (CNT/TPU) nanocomposites was printed by fused deposition modeling (FDM), and 1-pyrenecarboxylic acid (PCA) was introduced to non-covalently modify the CNTs and improve the polymer-nanofiller interactions. It is shown that the tensile and electrical properties of the modified composites are increased as a result of more uniform CNT dispersion. The 3D printed sensors demonstrate excellent properties

with high gauge factor (GF=117213 at a strain of 250%), large detectable strain (0~250%), good stability (up to 1000 loading/unloading cycles) and wide frequency response range of 0.01~1 Hz. Also, the strain sensing ability of the sensor is greatly improved with the introduction of PCA. The working mechanism of strain sensor was further studied based on the Simmons' tunneling theory. In addition, the sensor demonstrates the capability to monitor human body movements and voice, showing its potential for applications in intelligent robots and wearable electronics where customizability is demanded.

Keywords: 3D printing; interfacial interactions; sensor; carbon nanotubes; polymer nanocomposites

1. Introduction

Conductive polymer composites (CPCs) [1,2] have been reported in numerous literature as a result of their excellent processability and wide applications in advanced electronics, aerospace as well as in new energy areas etc. Carbon nanoparticles with high aspect ratios, such as CNTs and graphene, are the most favorable conductive nanofillers for fabricating CPCs when a low electrical percolation threshold is required [3]. The conductive pathways formed by conductive nanofillers in CPCs may be destroyed as strain is applied, resulting in a conductivity that is strain sensitive. Therefore, CPCs have the capability to behave as strain sensors. Strain sensors based on highly flexible CPCs have attracted widespread attention [4]. By way of example, Liu et al. [5] integrated genetically engineered cells as

programmable functional components with robust, elastic, and biocompatible hydrogel–elastomer hybrids to fabricate stretchable living materials and devices. Li et al. [6] manufactured strain sensors with high elasticity and sensitivity based on the composites of polydimethylsiloxane (PDMS) and 3D graphene foam. This sensor prepared by lyophilization can detect strains of 0~30%, and the sensitivity reaches 98.66 at 5% strain. Wang et al. [7] proposed an efficient strategy to produce stretchable strain sensors with excellent mechanical and conductive properties. Multi-walled CNTs were decorated onto the surface of electrospun polyamide 6 (PA6) nanofibers by an ultrasonication anchoring technique to produce a conductive network, which was then embedded into a polymer matrix to form a high-strength conductive composite. Although these strain sensors show good sensing performance, the fabrication approaches employed in their manufacture are usually quite complicated and unlikely to be scalable to industrial processing.

3D printing (namely additive manufacturing) is a rapid prototyping technology [8-10] that allows complex structures to be printed without the need for any mold tooling. This reduces capital costs and increases lead times as well as allowing the manufacture of structures that cannot be made by any other method. Currently, 3D printing has multiple classifications to meet different materials [11], such as metals and polymers by selective laser sintering, photocurable materials by stereolithghraphy, inkjet printing and thermoplastics by fused deposition modeling (FDM, namely Fused Filament Fabrication/FFF) [12].

In recent years, a lot of work has been carried out to develop the 3D printing

technology for polymer composites. Wei et al. [13] used the CNT/PDMS composite ink to directly print a freestanding wavy flexible electrode with high stretchability (>300% strain) and excellent electrical stability (about 5% resistance change at a strain of 100%). The effect of serpentine shape and connecting angle on the stretchability and conductivity of the electrode was systematically studied to optimize its performance. Compared with other 3D printing methods, fused deposition modeling has the characteristics of low cost, convenience and flexibility, and the extruded filaments are suitable for large-scale production and long-term storage. Christ et al. [14] developed a MWCNT/TPU as a raw material for FDM and printed a flexible circuit with high elasticity and excellent pressure sensitive properties. It was found that the content of MWCNTs had an important effect on its sensitivity and detectable range. Kim et al. [15] proposed a new approach to directly print 3D multiaxial force sensor using FDM based on functionalized composite filaments. The sensor had two components: the structural component was printed from thermoplastic polyurethane filaments, and the sensing component was printed from CNT/TPU nanocomposite filaments.

Although these studies have demonstrated the fabrication of flexible strain sensors by 3D printing technology, the interfacial properties of composites used for 3D printing are usually ignored. Interfacial interactions between the polymer and nanofiller play an important role in composites, significantly affecting the nanofiller dispersion in the matrix and the mechanical and physical properties of the composite material. If the interfacial properties can be tuned then so also can the performance of

the printed strain sensors. The methods to improve the interfacial properties of composites include non-covalent and covalent modifications. Covalent modification often destroys the intrinsic structure of nanofillers, which severely affects the mechanical and electrical properties of nanofillers. By contrast, non-covalent modification can enhance the interfacial interactions without sacrificing the unique structural and physical characteristics of nanofillers. However, few research on enhancing the sensing performance of flexible strain sensors via non-covalent interactions has been reported. Herein lies the motivation for this work.

In this work, CNT/TPU nanocomposites were prepared by solution mixing and extruded into filaments using a single-screw extruder for fabricating flexible strain sensors by FDM. Since π-π non-covalent interactions can be generated between CNTs and 1-pyrenecarboxylic acid (PCA) through a conjugation effect, and hydrogen bonding can also be formed between the carboxyl groups of PCA and the carbonyl and amide groups of TPU [16], PCA was used to non-covalently modify the nanotubes in order to improve their dispersion and alter polymer-nanofiller interactions without destruction of the intrinsic structure of the carbon nanotubes. The tensile, electrical and electromechanical properties of the 3D printed nanocomposites were also systematically investigated. It is observed that the strain sensors printed with non-covalent interactions exhibit better mechanical properties, electrical conductivity and strain sensing performance. This work provides important information for the fabrication of flexible and high-performance strain sensors using 3D printing technique when customizability, multi-directionality and complex design

are demanded. In addition, the non-covalent modification method of CNTs presented in this work can also be transferred to the preparation of polymer/CNT nanocomposites using more efficient and industrially favorable melt-mixing.

2. Experimental section

2.1. Materials

Multi-walled carbon nanotubes (NC7000) were purchased from Nanocyl SA (Belgium). The length of the CNT is about 1.5 μm and the diameter is 9.5 nm. 1-pyrenecarboxylic acid (PCA) with a density of 1.85 g/cm^3 was obtained from Aladdin Reagent Company (China). Thermoplastic polyurethane in powder form (Bayer 2195) was obtained from Bayer Co. Ltd. with a melt flow index of 12.1 g/10 min (205 °C, at a pressure of 5 kg) and a density of 1.19 g/cm^3 [26, 32]. Dimethylformamide (DMF) reagent was provided by Chengdu Kelong Chemical Reagent Company (China).

2.2. Preparation of CNT/TPU nanocomposites

Firstly, CNTs and PCA were dispersed in DMF via ultra-sonicating at 100 W for 1 hour at 25 □. The weight fraction ratio of CNTs to PCA was found to be optimized at 4:1 (Fig. S1 in the Supporting Information). TPU was dissolved in the resulting suspension with magnetic stirring for 2 hours (10 g TPU per 100 ml DMF). The mixed suspension was transferred into a glass mold (140 mm×140 mm×40 mm) to dry for 24 h at 100 °C in an air-circulating oven in order to produce nanocomposite sheets. It

should be noted that the nanocomposites without the addition of PCA were also prepared using the same method for comparison (Fig. 1a).

2.3. 3D printing of nanocomposites

The above nanocomposite sheets were cut into small granules and fed into a benchtop single-screw extruder (Wellzoom Type C) to manufacture filaments with a diameter of 1.75 mm suitable for FDM 3D printing. The operating temperature of the extruder was 190 ℃, and the screw speed was 100 rev/min.

CNT/TPU filaments were printed using an ET-K1 (ET Co. Ltd., China) desktop FDM 3D printer. A stacking mode was used with an interlayer angle of 90° (Fig 1.b). The FDM printing parameters are shown in Table 1. All the samples for tensile, electrical and electromechanical tests were printed under the same conditions. The detailed geometric dimensions of specimens for different characterizations are specified in section 2.4.
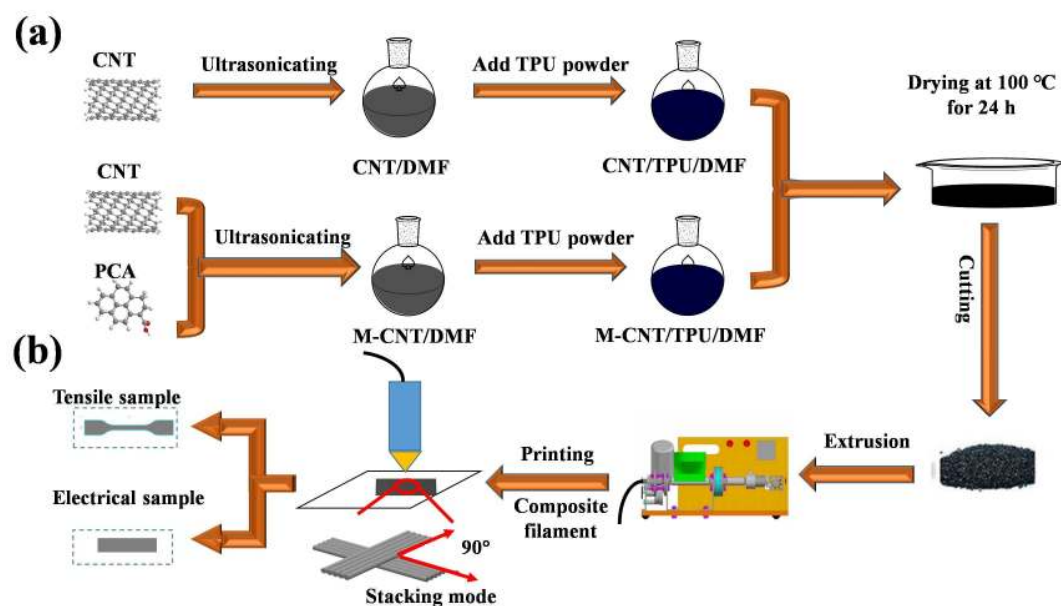
Fig. 1. Schematic of (a) preparation process of CNT/TPU nanocomposites and (b) 3D printing of the nanocomposites.

Table 1. 3D printing parameters for the CNT/TPU nanocomposites.

Parameter	Value
Nozzle diameter (mm)	0.4
Nozzle temperature (□)	220
Hot bed temperature (□)	70
Printing speed (mm/s)	20
Filling rate (%)	100
Layer thickness (mm)	0.1

2.4. Characterization

The dispersibility of CNTs modified (M-CNTs) and unmodified by PCA in DMF was tested using a Zeta potentiometer (Brookhaven Zeta PALS 190 Plus). Fourier-transform infrared spectroscopy (FTIR) using a WQF-520 FTIR spectrometer was conducted to verify the non-covalent interactions. Raman spectra were collected for the cast nanocomposites using an Ocean IM-52 spectrometer (excitation wavelength 785 nm) at a laser power of 78.4 mW. The fracture morphologies of cast and printed nanocomposites were examined by FESEM (FEI Quanta 650 FEG) under an accelerating voltage of 20 kV after gold sputtered.

Tensile tests were carried out for the nanocomposites using an MTS CMT4104 Universal Tester at room temperature (IOS 37: 1994). The dimensions of the

dumbbell specimen were 75 mm × 15 mm × 1 mm (Fig. 2a). Young's modulus was

determined using a clip-on extensometer with a gauge length of 20 mm at the speed of

200 mm/min.

The electrical resistivity (ρ) of the CNT/TPU nanocomposites was measured in

cross-layer and through-layer directions using a two-point method combined with a

DC digital source meter (Tektronix PWS4323) and picoamp-meter (Keithley 6485) at

3 V. The material strips had a dimension of 50 mm × 10 mm, and the electrode

distance was 15 mm (Fig. 2b). The resistivity of the nanocomposites was calculated

using Eq. (1):

$$\rho = R\frac{S}{L} \tag{1}$$

where R is the electrical resistance of the sample, L and S are the electrode

distance and cross-sectional area of the sample, respectively.
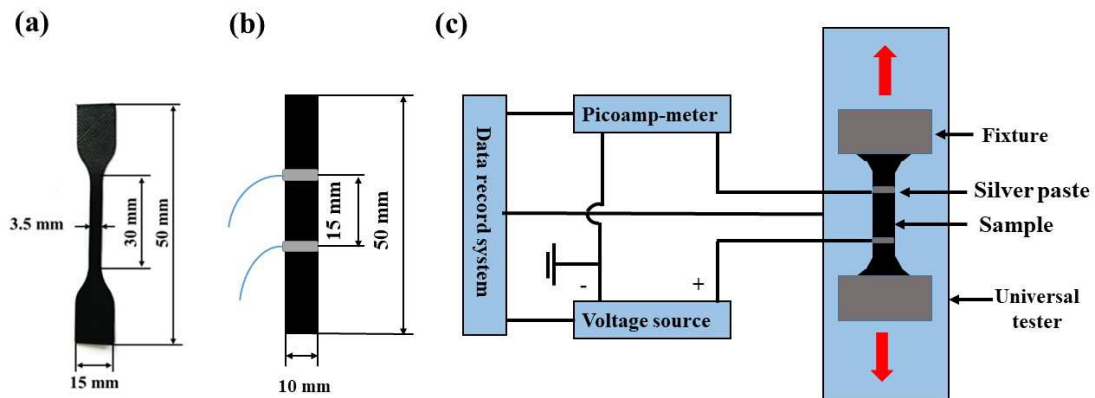

Fig. 2. Samples for (a) tensile and (b) electrical resistivity testing and (c) schematic for electromechanical testing.

The electromechanical performance of the printed strain sensors was measured

using the above universal tester, DC digital source meter and picoamp-meter at 3 V.

To more precisely characterize the relationship of strain and relative resistance change ($\Delta R/R_0$), the same dumbbell specimens for tensile testing were used, and the electrode distance was 20 mm (Fig. 2c).

3. Results and discussion

3.1. Dispersion and morphology

The Zeta potential ($|\varsigma|$) of the modified CNTs/DMF suspension was 49.6 mv compared with 17.3 mv for the unmodified CNT suspension [33]. This implies that the dispersion of the MWCNTs suspension is greatly improved by the addition of 1-pyrenecarboxylic acid [16]. To further study the dispersibility of CNTs, the CNT and M-CNT suspensions were left standing, after ultrasonication for 1 h, for a period of 30 days. As is shown in Fig. 3 that precipitation occurs for the unmodified CNT suspension after 15 days, while the M-CNT suspension still exhibits a good dispersion state after 30 days. This can be attributed to the fact that 1-pyrenecarboxylic acid adheres to the surface of the CNTs by physically forming a π-π stack, which enhances the electrostatic repulsive-forces between the CNT sidewalls [17].
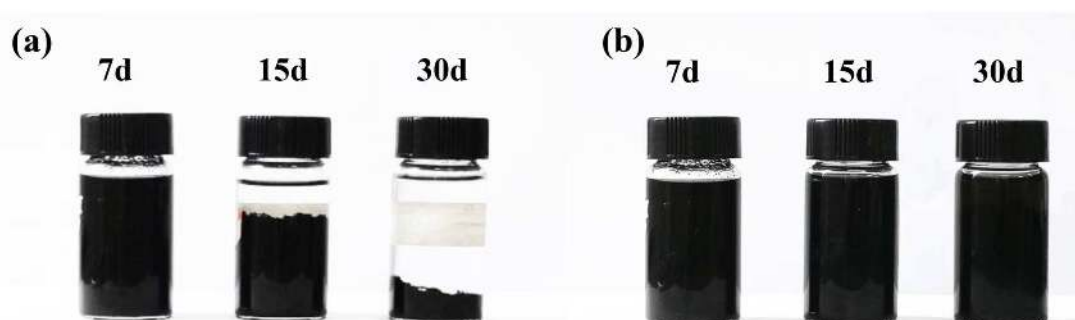

Fig. 3. Photographs of (a) unmodified and (b) modified CNTs suspension after standing for 7,

15 and 30 days respectively.

The morphologies of cast and 3D printed samples with 3 wt% MWCNTs were investigated by FESEM at different magnifications, as shown in Fig. 4. A clear multi-layer structure with a layer thickness of about 0.1 mm can be seen in the printed nanocomposites (Fig. 4b and c) compared with the cast nanocomposite (Fig. 4a). In addition, there are more voids in the printed samples in spite of good interlayer adhesion. It is observed in Fig. 4d and Fig. 4e that many small nanotube agglomerates are uniformly distributed in the cast and printed CNT/TPU nanocomposites, while there are very few agglomerates in the M-CNT/TPU nanocomposite (Fig. 4f). At a higher magnification, a better nanotube dispersion state for the M-CNT/TPU nanocomposite can be observed in Fig. 4i, compared with Fig. 4g and Fig. 4h. This demonstrates that the dispersion of CNTs in the TPU matrix is improved with the addition of PCA.
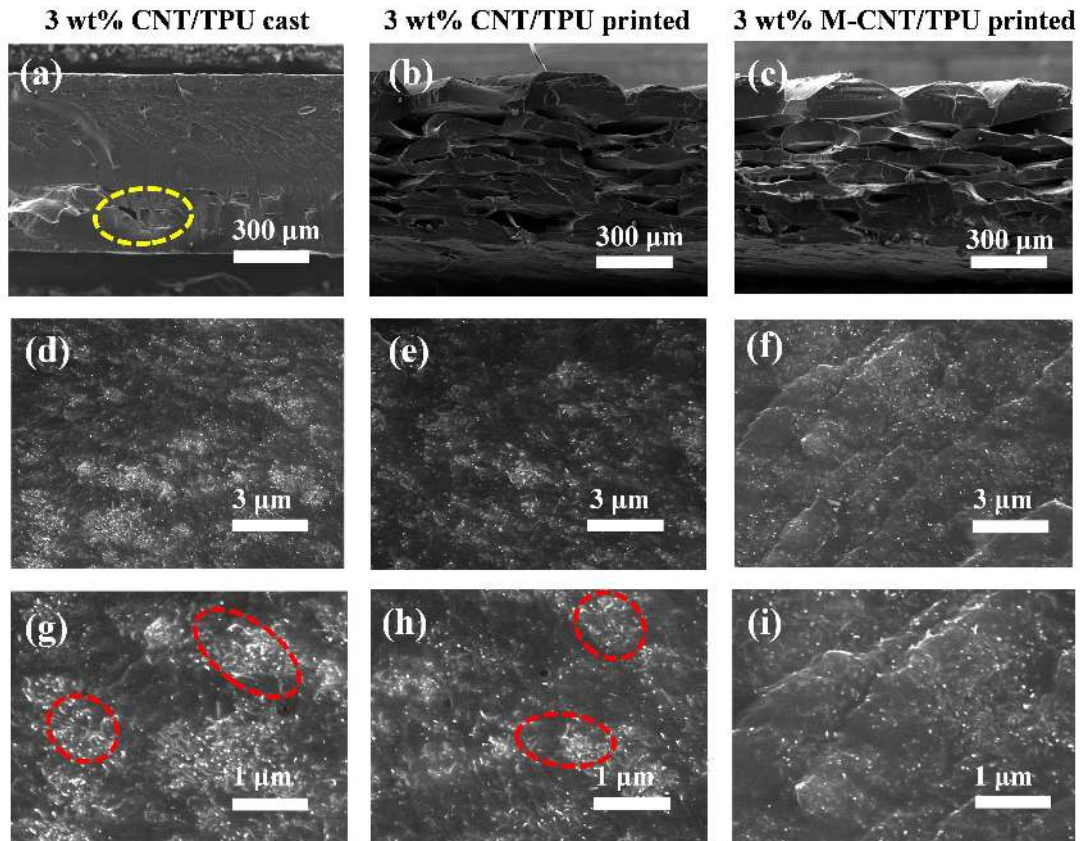
Fig. 4. SEM micrographs of fractured cross-sections for the cast and 3D printed samples with 3 wt% MWCNTs: (a, d, g) cast CNT/TPU nanocomposite, (b, e, h) printed CNT/TPU nanocomposite, (c, f, i) printed M-CNT/TPU nanocomposite. It should be noted that the red and yellow circles indicate the CNT agglomerates and voids, respectively.

3.2. Mechanical properties

The tensile properties of 3D printed and cast CNT/TPU nanocomposites are shown in Fig. 5 and Table 2. In general, it can be seen in Fig. 5 that all the nanocomposite samples exhibit similar strain-stress behavior, and strain hardening behavior can be observed when strain exceeds 200%. Comparing the 3 wt% CNT/TPU cast with the 3 wt% CNT/TPU printed nanocomposites, it can be observed that the printed samples have slightly better mechanical properties in general. This is

likely to be due to mild CNT disentanglement and alignment due to shearing in the single-screw extruder and printer nozzle. Disentanglement would reduce the extent of agglomeration and improve elongation while alignment would improve modulus and tensile strength. Comparing the modified with the unmodified printed material, increases of 27%, 68% and 19% for Young's modulus, tensile strength and elongation at break respectively are observed for the modified material at the same content of 3 wt%. The influence of CNT content is observed in increases of 39% and 49% in Young's modulus (43% and 52% in tensile strength) for the 3 wt% unmodified and modified materials respectively compared with the unfilled printed sample. Elongation at break is slightly increased for the 1.5 wt% sample relative to the unfilled material but a dropping in elongation from 703% to 601% occurs for the 3 wt% sample. This indicates that at 3 wt% CNT loading the material has some agglomeration which acts as a stress concentrator.

In general, the nanocomposite specimens with excellent mechanical properties were fabricated by 3D printing. The addition of PCA improves the dispersion of CNTs in the TPU matrix, which contributes to the further enhancement of the mechanical properties of the nanocomposites. It should be noted that 3D printing can achieve different filament alignments by controlling the printing paths (Fig. S2), which has a significant impact on the tensile properties of the composite materials (Fig. S3 and Table S1). Herein, we applied the optimized printing path to fabricate the strain sensors.
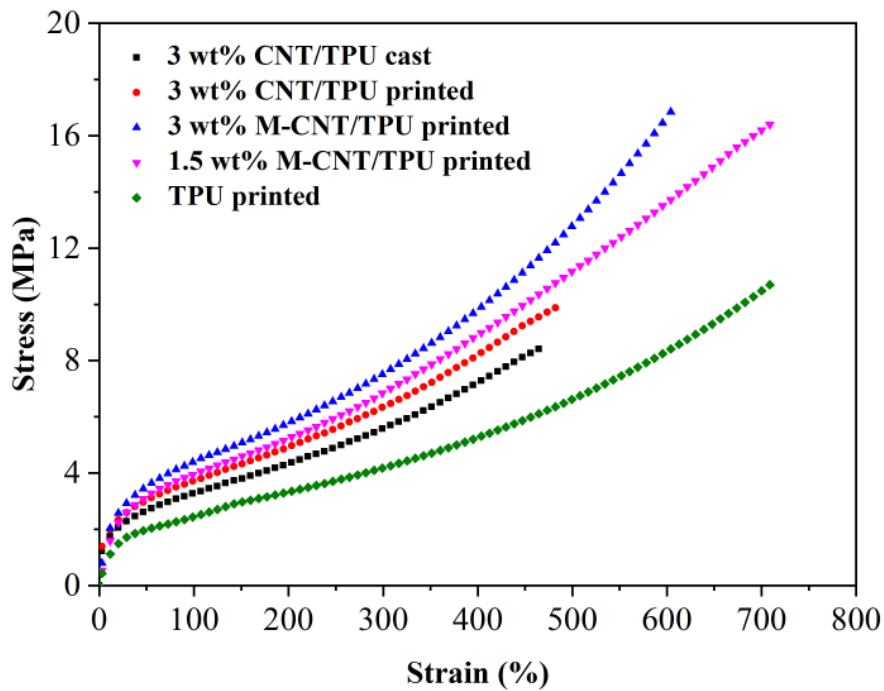
Fig. 5. Typical strain-stress curves for the CNT/TPU nanocomposites.

Table 2. Tensile properties of the CNT/TPU nanocomposites.

Sample	E (MPa)	σ (MPa)	ε_b (%)
3 wt% CNT/TPU cast	15.1±0.7	8.0±0.6	465.7±14.4
3 wt% CNT/TPU printed	17.1±0.8	10.4±0.4	505.3±16.3
3 wt% M-CNT/TPU printed	21.7±2.9	17.5±0.6	601.2±21.4
1.5 wt% M-CNT/TPU printed	20.3±0.9	16.5±0.6	710.4±23.0
TPU printed	14.6±0.8	11.5±0.6	703.6±11.9

In order to explore the changes in interfacial interactions with the addition of

PCA, FTIR and Raman tests were analyzed for the 3D printed samples with 3 wt%

unmodified and modified CNTs, as shown in Fig. 6. From FTIR spectra (Fig. 6a), the

characteristic peak at the 1754 cm^{-1} wavenumber corresponds to carbonyl groups in

the polymer chains, and the peak at the 1544 cm^{-1} is led by the deformation and

vibration of amide groups [18]. The characteristic peak of the adipose group is

observed at 1106 cm^{-1}. Compared with the CNT/TPU nanocomposite, the full width at

half maximum of the carbonyl peak of M-CNT/TPU at 1754 cm^{-1} is significantly

increased. This demonstrates the formation of strong hydrogen bonding between the carbonyl and amide groups of TPU and the carboxyl groups of PCA. In addition, it can be seen in Fig. 6a that the M-CNT/TPU nanocomposite exhibits a small single peak at 880 cm^{-1}, which is the characteristic peak of 5 substituted benzene in PCA. The low intensity of this peak can be attributed to the very small addition of PCA (about 0.6 wt%). Fig. 6b shows the Raman spectra of CNT/TPU and M-CNT/TPU nanocomposites. The D-band is derived from the disordered graphite structure and the G-band is derived from the in-plane vibration of C-C bonds [18]. The D-band and G-band of M-CNT/TPU samples are 1305 cm^{-1} and 1611 cm^{-1} in Fig. 6b, respectively, which are 25 cm^{-1} and 22 cm^{-1} higher than those of CNT/TPU samples [19]. Both the D-band and the G-band show a significant right shift, indicating that the modified nanocomposites have higher interfacial forces. The peak strengths of the G-band and D-band are denoted as I_D and I_G, respectively. The I_D/I_G values for CNT/TPU ($I_{D1}/I_{G1} = 1.071$) and M-CNT/TPU ($I_{D2}/I_{G2}=1.083$) nanocomposites are not significantly changed, indicating that the pristine structure of CNTs is not damaged by the non-covalent modification.
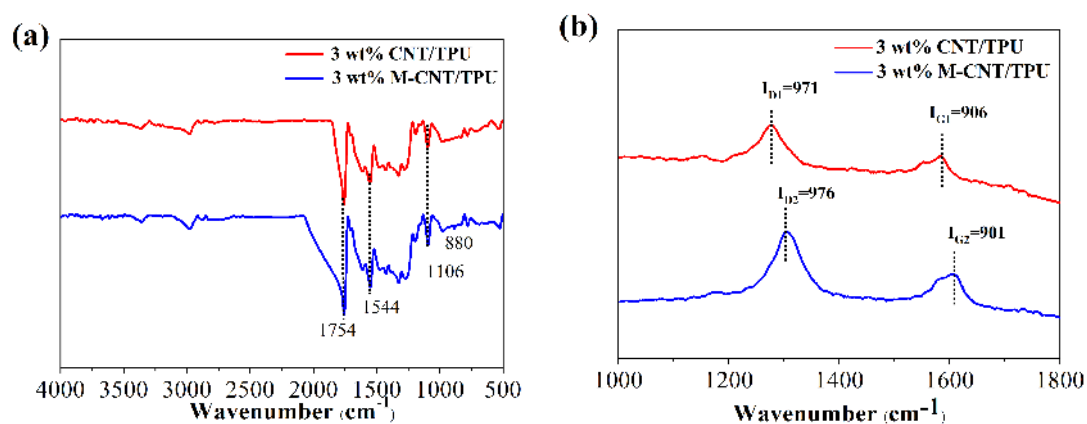

Fig. 6. (a) FTIR and (b) Raman spectra of the CNT/TPU and M-CNT/TPU nanocomposites.

3.3.   Electrical properties

The electrical resistivity, in different directions, of cast and printed nanocomposites is shown in Table 3. It can be seen that the forming method has a great influence on the resistivity of material with resistivity increasing in both directions in the printed material. In the cross-layer direction, the resistivity of the printed sample is nearly 20 times higher than that of the cast sample with the same 3 wt% CNT addition. This can be attributed to the orientation of the CNTs during extrusion and 3D printing which results in the reorganization of the conductive network structure with preferential alignment in the extrusion/print direction. Greater alignment in the print direction accounts for the lower resistivity in the cross-layer (print direction) than in the through-layer direction. However, the orientation degree of nanotubes may be not very significant, considering the relatively small shear forces during 3D printing [14]. The addition of PCA results in a 37 fold drop in resistivity of the printed material compared with the unmodified 3 wt% CNT/TPU material and the modified material resistivity is also more sensitive to direction due to the enhanced dispersion of CNTs. Comparing the modified material containing 3 wt% CNTs with that containing 1.5 wt% CNT we observe an increase in resistivity of approximately one order of magnitude which is to be expected as there are fewer CNTs in the network. However, the modified material containing 1.5 wt% CNTs is still somewhat lower in resistivity that the unmodified material containing 3 wt% CNTs so the modification allows the same electrical performance for half the CNT content. It should be noted that the printed 1.5 wt% CNT/TPU sample without the addition of

PCA is nonconductive, thus it is not presented in this work. As shown in Fig. S4, according to classic percolation theory, the percolation threshold (fc) of the printed CNT/TPU nanocomposites is 1.98 wt%. Furthermore, the addition of PCA can effectively reduce the CNT percolation loading in nanocomposites. When the weight fraction ratio of CNT to PCA is 4:1, the percolation threshold of the printed nanocomposites is reduced to 0.95 wt%. In addition, the printing path also influences the electrical properties of the composite materials (Table S2).

Table 3. The resistivity of nanocomposite materials in different directions.

Sample	Resistivity ($\Omega \cdot m$)	
	Cross-layer	Through-layer
3 wt% CNT/TPU cast	2.247×10^2	2.253×10^2
3 wt% CNT/TPU printed	4.285×10^3	1.516×10^4
3 wt% M-CNT/TPU printed	1.151×10^2	5.730×10^2
1.5 wt% M-CNT/TPU printed	1.765×10^3	1.059×10^4

3.4. Electromechanical performance

Electromechanical performance of the cast and 3D printed samples was carried out by measuring the resistance under monodirectional stretching and cyclic loading/unloading. The sensitivity of the sensor is usually expressed by a guage factor (GF) calculated using Eq. (2):

$$\text{GF} = \frac{\Delta R}{R_0 \times \Delta \varepsilon} \tag{2}$$

Where $\Delta \varepsilon$, ΔR and R_0 represent the applied strain, resistance change under strain

and initial resistance, respectively [20]. When the CNT content is 3 wt%, the printed

sensor has both high sensitivity and large strain response range (Fig.S5). Fig. 7 shows

the relationship between the $\Delta R/R_0$ and tensile strain for different samples. The $\Delta R/R_0$

of the 3D printed sensors steadily increases with increasing strain, suggesting a clear

electromechanical response. Moreover, all sensors have high linearity at low strains

and excellent strain monitoring capabilities (over 250%). It can clearly be seen that the

printed 3 wt% M-CNT/TPU sample exhibits a higher sensitivity over the whole strain

range compared with the printed 3 wt% CNT/TPU. When the strain is less than 20%,

the sensitivity increases from 2.53 to 3.21 with the addition of PCA. When the strain

reaches 250%, The sensitivity (GF_3) of the printed 3 wt% M-CNT/TPU is nearly 7

times higher than that (GF_2) of the printed 3 wt% CNT/TPU. In addition, a lower

concentration of M-CNTs in the printed sensor contributes to a higher sensitivity, with

the 1.5 wt% M-CNT sensor having the highest sensitivity regardless of the strain range.

Generally, one can see in Fig. 7 that $GF_1 < GF_2 < GF_3 < GF_4$. As expected, the printing

path also has a significant effect on the electromechanical response of the

nanocomposites (Fig. S3). Besides, the addition of PCA is also beneficial to the

sensitivity of the cast sensor (Fig. S6). Compared with the recently reported literature,

the printed sensor (1.5 wt% M-CNT/TPU) in our work exhibits an outstanding

performance in both sensitivity and detectable strain range (Fig. 8) [20-28].
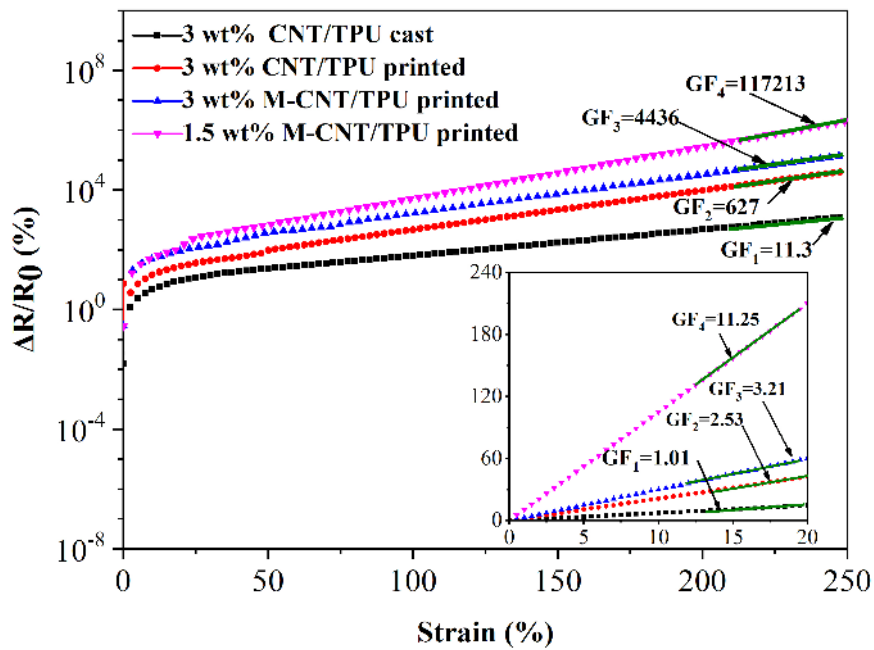
Fig. 7. $\Delta R/R_0$ as a function of strain for the strain sensors with different CNT contents and
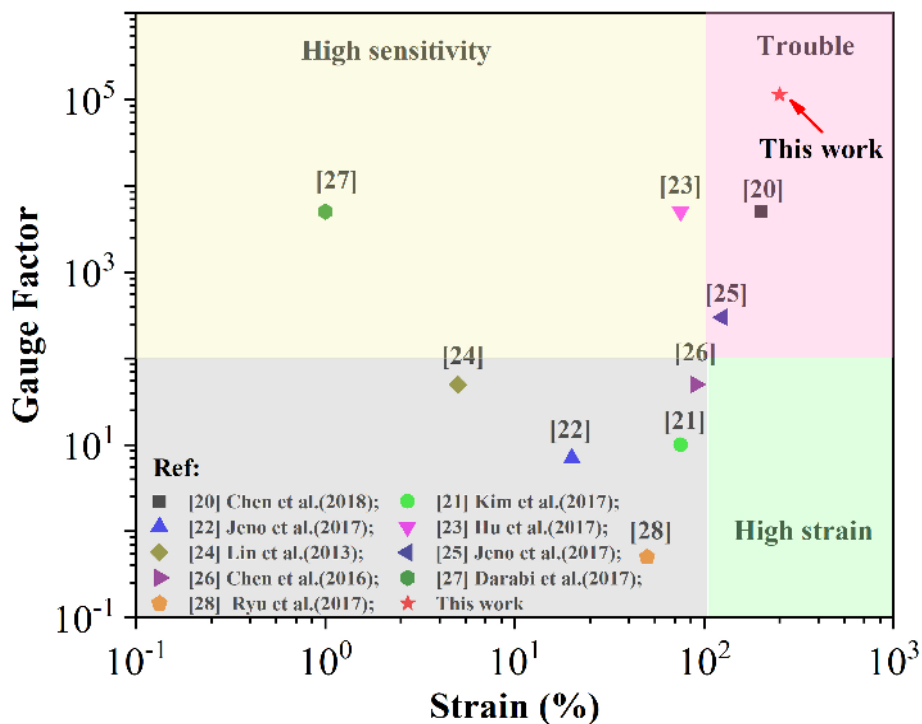
processing methods.

Fig 8. Comparison of the gauge factor and detectable strain range of the printed strain sensor

with that of recently reported strain sensors.

The sensing performance of the sensors were also tested at different strains when the frequency was 0.1 Hz. From Fig. 9, the relative resistance change of the sensors regularly responds to the applied strains, indicating that the sensors enable to detect multiple deformations. As expected, the printed 1.5 wt% M-CNT/TPU and cast 3 wt% CNT/TPU samples exhibit the strongest and weakest signal feedback at all the testing strains. Double peaks in the $\Delta R/R_0$ of nanocomposites during monotonic loading are rarely observed in literature, while they are usually observed during cyclic loading (Fig. 9). The competition between the destruction and reconstruction of conductive network during the loading/unloading process determines this behavior [29]. Mechanical hysteresis could explain it whereby the retraction of the macromolecular chains results in the reconstruction of some comductive pathways after the large deformation. However, the macromolecular chains cannot completely return to their original location after unloading. This hesteresis causes a destruction of the conductive network formed by the nanotubes, leading to more obvious shoulder peaks with increasing strain [30].
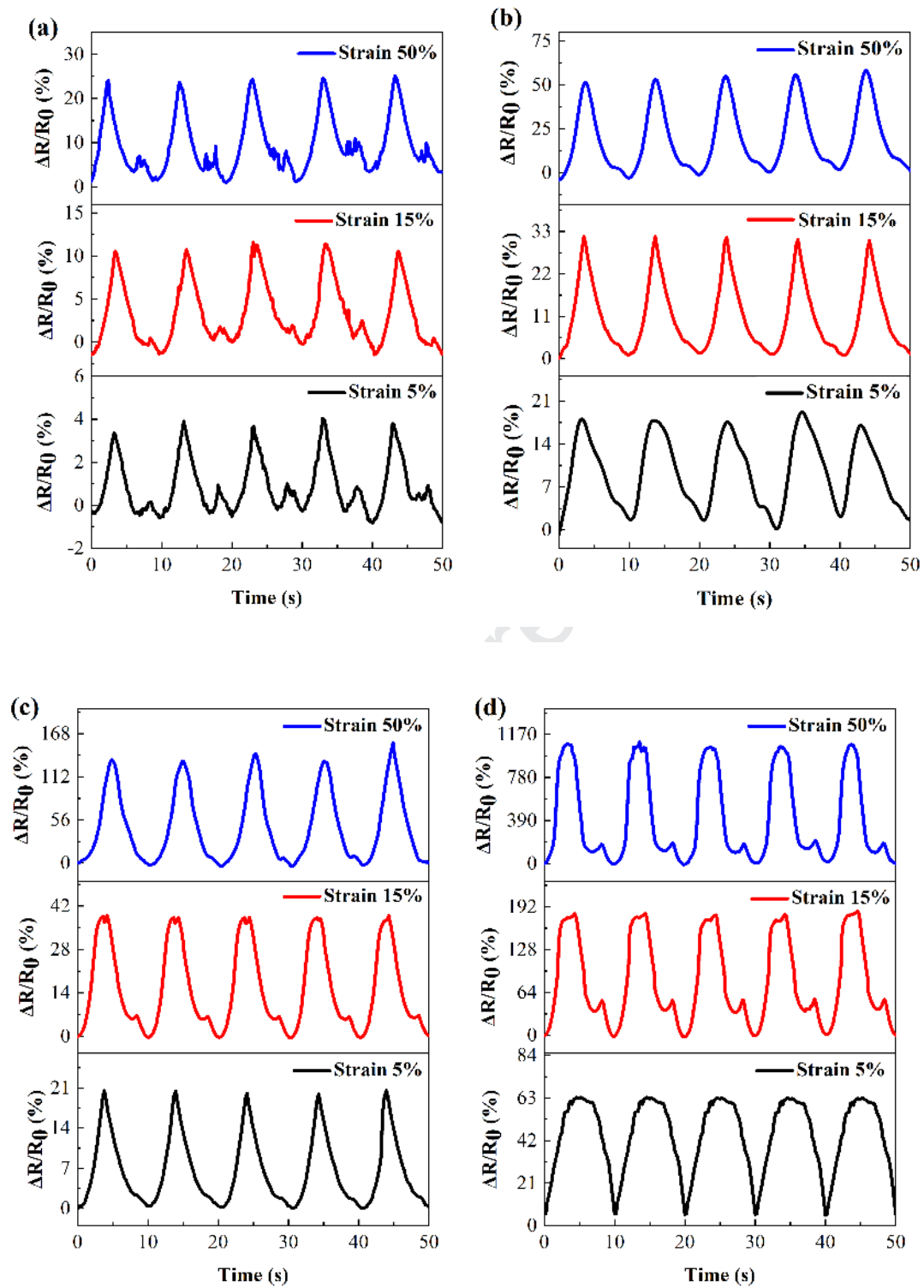
Fig. 9. $\Delta R/R_0$ of the strain sensors under cyclic loading at different strains (5%, 15%, 50%) and a frequency of 0.1 Hz: (a) 3 wt% CNT/TPU cast, (b) 3 wt% CNT/TPU printed, (c) 3 wt% M-CNT/TPU printed, (d) 1.5 wt% M-CNT/TPU printed.

The stress-strain relationship of the sensors may vary significantly when repeatedly loaded to large strains, thus their electromechanical responses ($\Delta R/R_0$-strain relationship) may also be affected. From Figures 10a and 11a, the printed sensor exhibited good recovery at low strain (30%), where the movement of the TPU molecular chains is hardly affected by viscoelasticity. Moreover, with the addition of PCA, the hysteresis in $\Delta R/R_0$-strain curves of the 3 wt % M-CNT/TPU printed sensor under low strain is smaller than that of 3 wt % CNT/TPU printed sensor (Fig. 10d and Fig. 11d). When the strain is increased to 100% and 250%, the printed sensors show more evident mechanical and electromechanical hysteresis. This is mainly due to strain softening [31] and the Mullins effect [32] in the tensile process of TPU and TPU based composites [14]. The strain softening effect in elastic polymers is related to the rearrangement of molecular chains to minimize the deformation energy as well as the physical breakage of the polymer matrix under large strains. The Mullins effect is generally considered as the change in elastic behavior of material, usually referred to as stress-softening, resulting from initial loadings. As shown in Fig. 10 b,c and Fig.11 b,c, the stress-strain curves of printed 3 wt% CNT/TPU and 3 wt% M-CNT/TPU sensors present a large change in the first cycle under large strains ($\varepsilon > 100\%$), but they tend to be stable after 10 cycles. The mechanical hysteresis in stretching-releasing cycles at different strains is calculated based on the area of the curves. From Fig. S7, the printed 3 wt% M-CNT/TPU sensor has lower mechanical hysteresis compared to the 3 wt% CNT/TPU sensor due to the enhanced interfacial interaction between the CNTs and TPU by non-covalent modification. A similar phenomenon can also be observed

in the $\Delta R/R_0$-strain relationship of the sensors at large strains. From Fig. 10 e,f and Fig. 11 e,f, the $\Delta R/R_0$-strain curves of the 3 wt% CNT/TPU printed sensor are clearly modified in the cyclic stretching-releasing process, while those of 3 wt% M-CNT/TPU printed sensor tend to stabilize after 10~100 cycles. Furthermore, the percentage change in $\Delta R/R_0$ for the 3 wt% M-CNT/TPU printed sensor (31.2%) during cyclic stretching is less than that for the 3 wt% CNT/TPU printed sensor (51.2%) at 250% strain, indicating that the addition of PCA has a positive effect on the stability of the sensor under large strains.
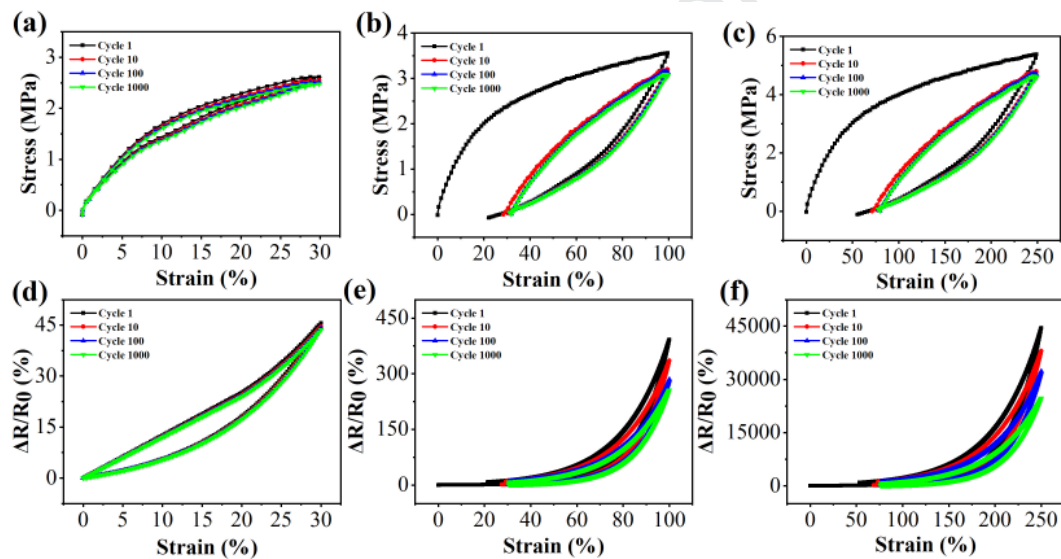

Fig. 10. Stress-strain and $\Delta R/R_0$-strain curves of 3 wt% CNT/TPU printed sensors during loading to different strains (30%, 100%, 250%) for 1000 cycles: (a, d) strain=30%, (c, e) strain=100% (d, f) strain=250%.

Fig. 11. Stress-strain and $\Delta R/R_0$-strain curves of 3 wt% M-CNT/TPU printed sensors during loading to different strains (30%, 100%, 250%) for 1000 cycles: (a, d) strain=30%, (c, e) strain=100% (d, f) strain=250%.
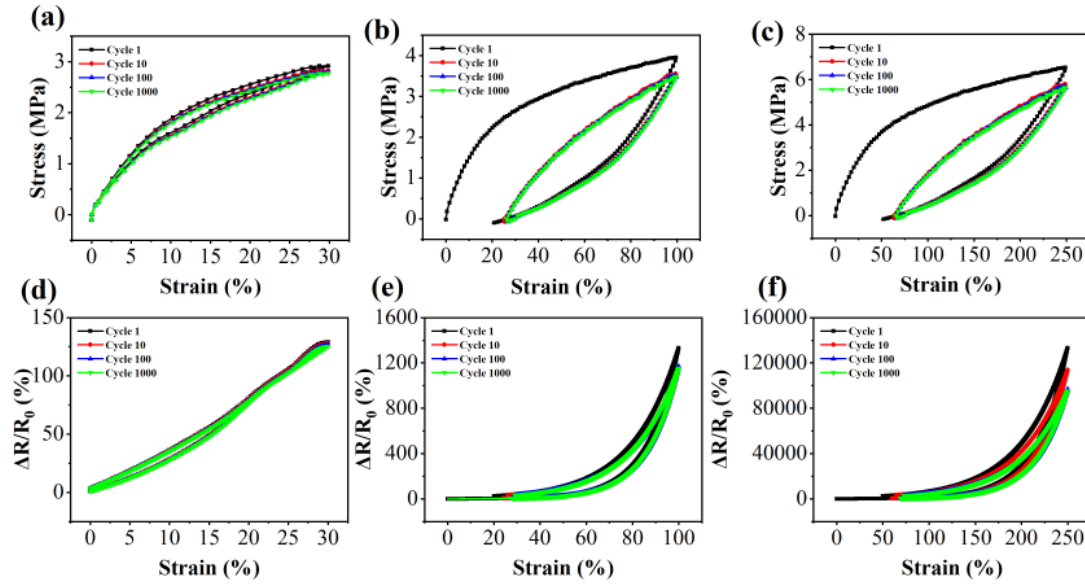
The $\Delta R/R_0$ of the 3D printed sensors under the same strain ($\varepsilon = 10\%$) and different frequencies (f = 1, 0.1, 0.2, 0.01 Hz) was also investigated, as shown in Fig. 12. The strain sensors demonstrate the capability of detecting strain within a broad frequency range. It can be seen that the $\Delta R/R_0$ of sensors increases with increasing frequency, which is mainly due to the decrease in the molecular mobility at a high frequency resulting in a stiffer mechanical response [33].
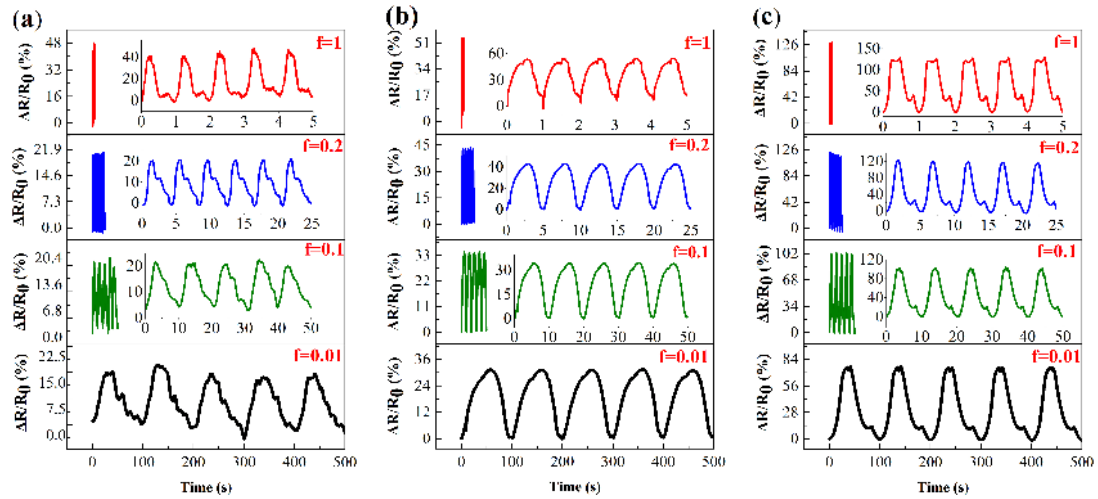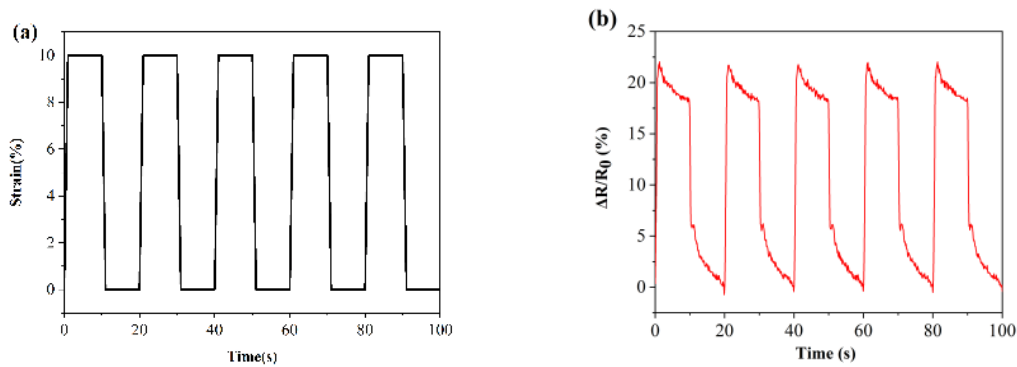
Fig. 12. $\Delta R/R_0$ of the 3D printed strain sensors during a cyclic loading at a strain of 10% and a frequency of 0.01, 0.1, 0.2, 1 Hz: (a) 3 wt% CNT/TPU, (b) 3 wt% M-CNT/TPU, (c) 1.5 wt% M-CNT/TPU.

In order to further explore the relationship between sensing signal and strain, rectangular strain wave (ε = 10%, f = 0.05) testing was performed (Fig. 13a). One can see that the $\Delta R/R_0$ of all the sensors changes with time/strain, while the printed 3 wt% M-CNT/TPU (Fig. 13c) and 1.5 wt% M-CNT/TPU samples (Fig. 13d) show a better correlation compared with the printed 3 wt% CNT/TPU (Fig.13b), indicating that the enhanced interfacial interations leads to a higher sensitivity [34].
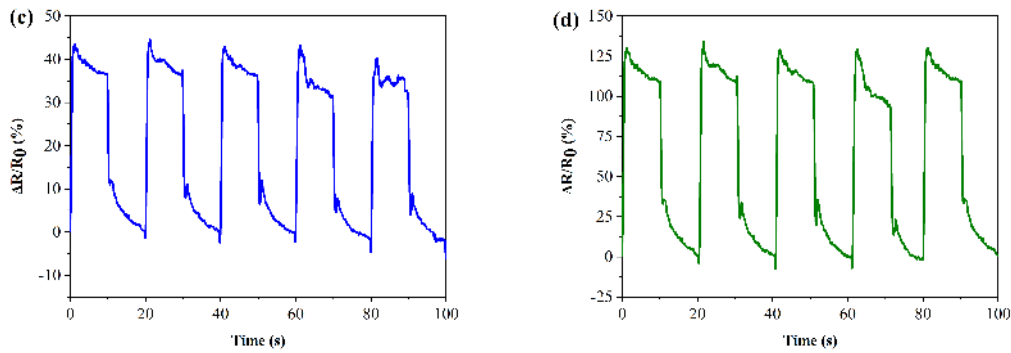
Fig. 13. $\Delta R/R_0$ of the 3D printed strain sensors under rectangular wave: (a) time-strain curve, (b) 3 wt% CNT/TPU, (c) 3 wt% M-CNT/TPU, (d) 1.5 wt% M-CNT/TPU.

The relative resistance changes of the printed sensors during 1000 loading/unloading cycles at different strains and a frequency of 1 Hz are shown in Fig. 14. It can be seen in Fig. 14a-c that all the printed strain sensors show excellent stability even after 1000 loading/unloading cycles. However, compared with the strain sensors of 3 wt% and 1.5 wt% M-CNT/TPU nanocomposites, theunmodified 3 wt% CNT/TPU sensor shows a clear upward shift after 700 cycles, indicating that the stability of sensors based on M-CNT/TPU is higher. In addition, it can be seen in Fig. 14d-f that the $\Delta R/R_0$ of the sensors with modified CNTs gradually stabilizes after the first 100 loading cycles at 250% strain. However, the printed sensor with unmodified CNTs exhibit a more evident instability in $\Delta R/R_0$ during the cyclic large strain tests. Therefore, the non-covalent modification can significantly improve the stability of the sensor due to stronger interfacial interactions between CNTs and TPU regardless of the strain range.
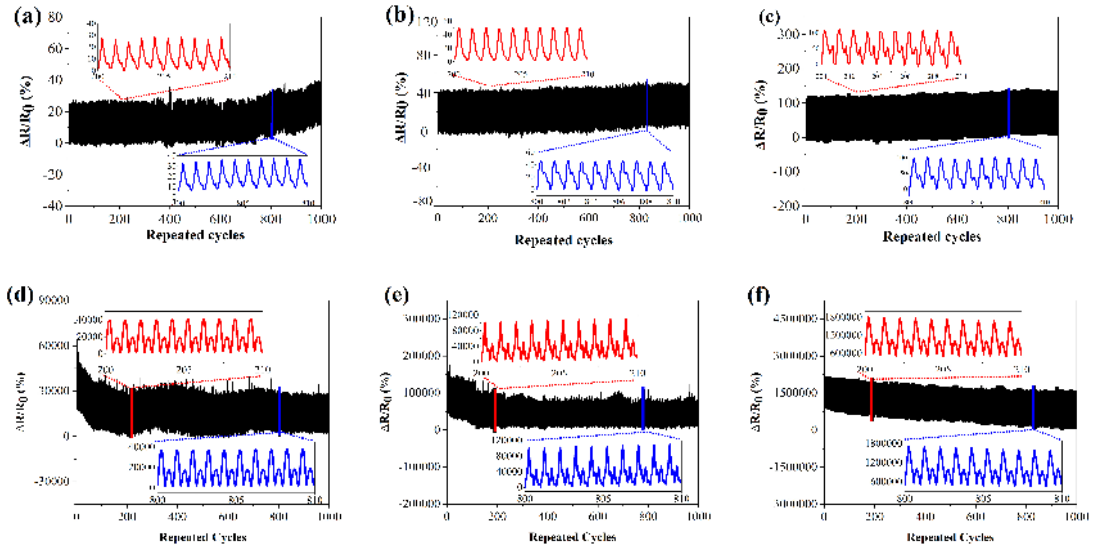
Fig. 14. $\Delta R/R_0$ of the 3D printed strain sensors during 1000 cycles at a strain of 10% and a frequency of 1 Hz: (a) 3 wt% CNT/TPU, (b) 3 wt% M-CNT/TPU, (c) 1.5 wt% M-CNT/TPU; $\Delta R/R_0$ of the 3D printed strain sensors during 1000 cycles at a strain of 250% and a frequency of 1 Hz: (d) 3 wt% CNT/TPU, (e) 3 wt% M-CNT/TPU, (f) 1.5 wt% M-CNT/TPU.

3.5. Modeling and mechanism

As mentioned earlier, the strain sensing response of the printed sensors greatly depends on the destruction and reformation of the conductive network. Based on Simmons' tunneling theory, a conductive model was established to study the sensing mechanism [20]. The total resistance R of conductive composites can be expressed by Eq. (3):

$$R = \left(\frac{L}{N}\right)\left(\frac{8\pi hs}{3\gamma a^2 e^2}\right)\exp(\gamma s) \tag{3}$$

$$\gamma = \frac{4\pi\sqrt{2m\varphi}}{h} \tag{4}$$

where L is the number of particles forming a single conductive path, N the number of conductive paths, h the Planck's constant, s the shortest distance between

conductive particles, a^2 the effective cross-section area, e the electron charge, m the electron mass, and φ the height of the potential barrier between particles [35].

When the composite is stretched, the distance between the nanofillers linearly increases from s_0 to s, which increases the electrical resistance of the composite. The shortest distance between nanofillers is calculated as follows:

$$s = s_0 \left(1 + C\left(\frac{\Delta l}{l_0}\right) \right) = s_0(1 + C\varepsilon) \tag{5}$$

where ε is the strain of the sensor, l_0 is the original length of the sensor, and Δl is the deformation of the sensor, and constant C varies with the material systems.

At large strains, a non-linear change in the number of conductive paths (N) results in a non-linear increase in resistance, which can be expressed by Eq. (6):

$$N = \frac{N_\circ}{\exp(M\varepsilon + W\varepsilon^2 + U\varepsilon^3 + V\varepsilon^4)} \tag{6}$$

where M, W, U, V are constants.

Substituting Eq. (6) and Eq. (5) into Eq. (3) gives Eq. (7):

$$R = B(1 + C\varepsilon)\exp[A + (M + AC)\varepsilon + W\varepsilon^2 + U\varepsilon^3 + V\varepsilon^4] \tag{7}$$

where A= γs_0, B= $\frac{8\pi hns_0}{3\gamma N_0^2 e^2 a^2}$, and n represents the total number of particles (n=L×N).

It can be observed in Figure 15 that the theoretical model agrees with the experimental results well. The fitting parameters A, B, C, M, W, U, and V are shown in Table 4. Fig. 16a and Fig. 16b, demonstrate the variations in tunneling distance (change of TD, y= Cx) and conductive paths (change of CP, y= $Mx+Wx^2+Ux^3+Vx^4$). In general, the change of TD linearly increases with increasing strain. Obviously, the changes of TD and CP in the printed 1.5 wt% M-CNT/TPU increase more evidently

compared with the printed 3 wt% M-CNT/TPU. This indicates that the sensitivity of the printed sensor increases as the CNT content decreases. Besides, the changes of TD and CP of the sensor after non-covalent bond modification also significantly increase at the same CNT content of 3 wt%. This indicates that the conductive network in the modified samples with stronger interfacial interactions is significantly deformed and is more readily destroyed under stretching.
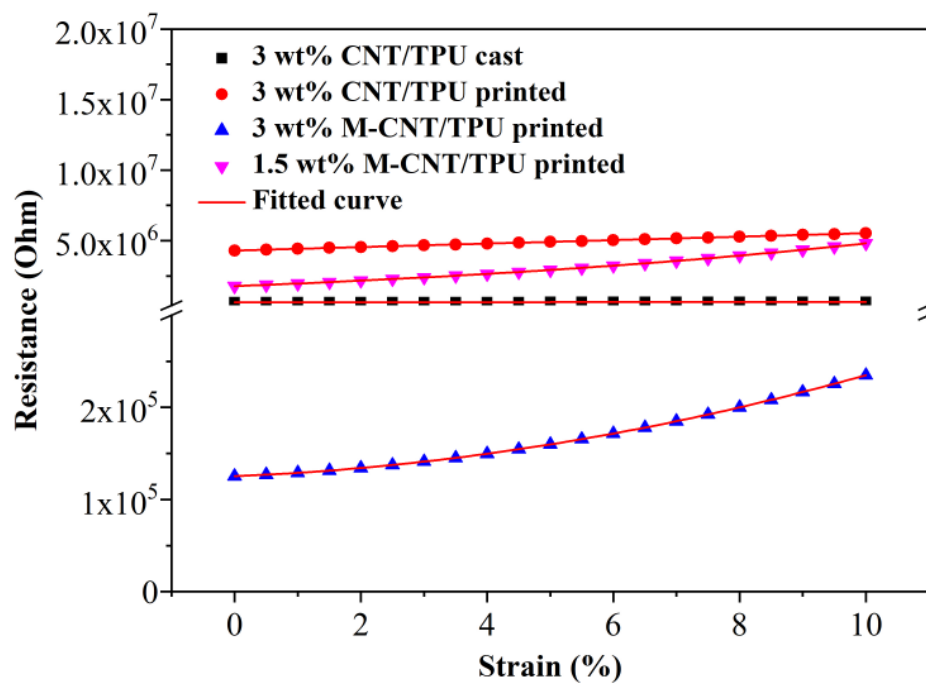

Fig. 15． Theoretical (red solid lines) and experimental (dots) results for the resistance-strain relationship of the printed sensors.
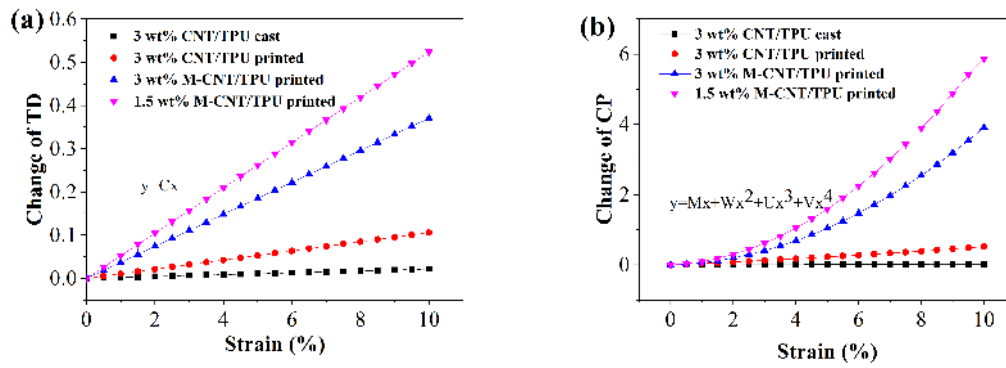
Fig. 16. Changes of the (a) tunneling distance and (b) the conductive paths against strain for
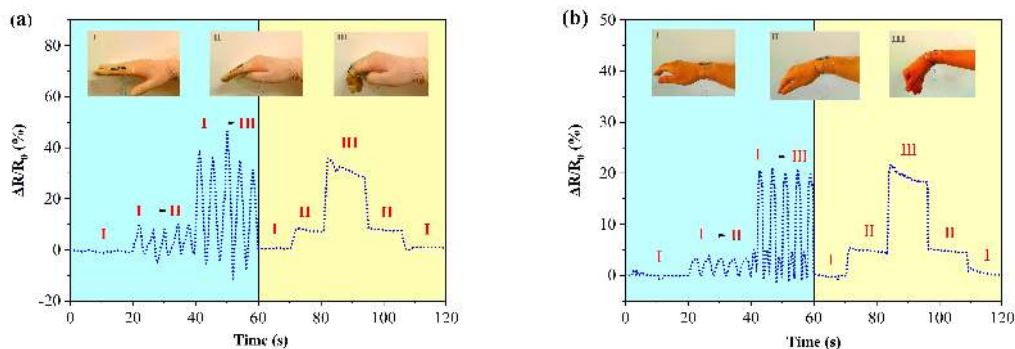
the printed sensors.

Table. 4. Parameters obtained from fitting the resistance-strain data.

Samples	3 wt% CNT/TPU casted	3 wt% CNT/TPU printed	3 wt% M-CNT/TPU printed	1.5 wt% M-CNT/TPU printed
A	0.0888	0.435	0.0481	0.133
B	5.72×10^5	2.78×10^6	1.31×10^5	2.03×10^6
C	0.00217	0.0136	0.0370	0.0547
M	0.00238	0.00385	0.0265	0.0570
W	-4.81×10^{-6}	0.00130	0.0365	0.0426
U	-3.69×10^{-6}	-5.16×10^{-7}	6.19×10^{-6}	0.0027
V	8.18×10^{-6}	4.03×10^{-7}	7.13×10^{-8}	-0.0002

3.6.   Applications

Due to the excellent performance in sensitivity and stability, the printed strain

sensors with 1.5 wt% modified CNTs could have a promising propective for flexible

electronic devices and health monitoring. Some application in detecting human

motions, such as finger movement, wrist bending, and breathing, were evaluated for the sensors and the results are illustrated in Fig. 17. When the strain sensor was attached to the index finger, bending of the finger could accurately be monitored with specific responses to different bending degrees (Fig. 17a). For example, $\Delta R/R_0$ reached 8.5% at a bending angle of 45°, and it increased to 35% at a bending angle of 90°. Fig. 17b demonstrates the response of the printed sensor to wrist bending. The $\Delta R/R_0$ response was 7.5% at a bending angle of 30°, and it increased to 20% at a bending angle of 60°. As the muscles of the abdomen change during breathing, this sensor can be used to detect changes in the frequency of breathing. As shown in Fig. 17c, the normal respiratory rate was about 0.33 Hz, which increased to 0.5 Hz after strenuous exercise with the corresponding $\Delta R/R_0$ increased by 2 times. As a result of the high flexibility and sensitivity of the sensor, it can be attached to the throat and used to monitor human speech (Fig. 17d). When the volunteer spoke different English words, the sensor outputed distinct signal patterns due to the delicate muscle movement leading to the changes of the conductive paths in the sensor [36].
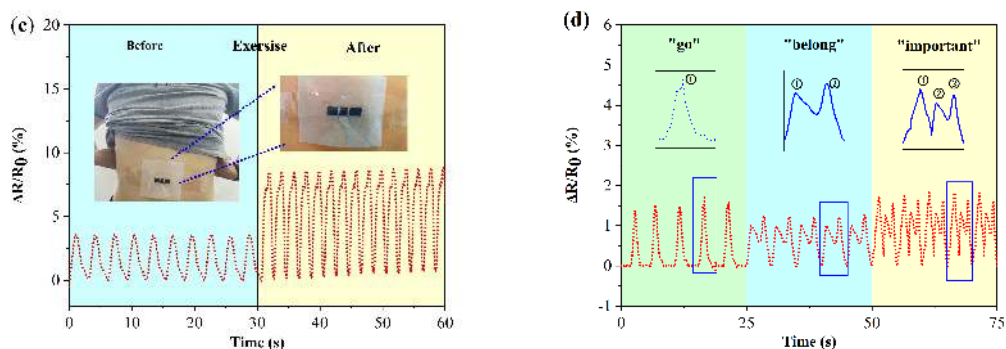
Fig. 17. Electromechanical responses of the printed sensor to (a) bending and unbending of index finger at 30°and 90, (b) wrist, (c) breathing and (d) speaking "go", "belong", and "important".

4. Conclusions

In this study, highly flexible strain sensors of CNT/TPU nanocomposites were fabricated by 3D printing, and 1-pyrenecarboxylic acid was introduced to non-covalently modify the CNTs and enhance the interfacial interactions. One can see that the dispersibility of the CNTs in the TPU matrix is improved with the introduction of PCA and this is accompanied by significantly improved tensile and electrical properties of the 3D printed sensors. The 3D printed 1.5 wt% M-CNT/TPU nanocomposite exhibited higher tensile modulus (20.3 MPa) and strength (16.5 MPa) and comparative elongation (710%) relative to the printed neat TPU sample. Compared with the printed 3 wt% CNT/TPU nanocomposite, the resistivity of M-CNT/TPU decreased by 37 times in the cross-layer direction at the same CNT loading. The sensor exhibited a high sensitivity (GF = 117213 at a strain of 250% for the printed sensor of 1.5wt% M-CNT/TPU) and a large detectable strain. Besides, the sensor performs well in the frequency range of 0.01~1Hz and shows the capability to

monitor the strains with different frequencies. Both strain softening and Mullins effect can be observed for the printed sensors, while the stress-strain and $\Delta R/R_0$-strain relationships tend to stablize after a few strain cycles. In addition, this sensor shows excellent stability during the cyclic strain testing up to 1000 cycles. The strain sensing properties of the sensor are greatly improved by the strong non-covalent interactions due to the introduction of PCA. A modeling study based on tunneling theory was carried out to understand the strain sensing mechanism, and the theoretical results agreed well with the experimental data. We also demonstrated the sensor's capability in monitoring human motions, including finger movements, joint movements, respiratory frequency, and speech recognition. This work provides a guideline for producing 3D printed high-performance flexible strain sensors with potential applications in intelligent robots, prosthetics and wearable devices where customizability and complex design are demanded.

Acknowledgements

References

[1]   Wang J, Wang W, Zhang C, Yu W. The electro-mechanical behavior of

conductive filler reinforced polymer composite undergone large deformation: A combined numerical-analytical study. Compos Part B Eng 2018;133:185–192. doi:10.1016/j.compositesb.2017.09.041.

[2] Vertuccio L, Guadagno L, Spinelli G, Lamberti P, Zarrelli M, Russo S, et al. Smart coatings of epoxy based CNTs designed to meet practical expectations in aeronautics. Compos Part B Eng 2018;147:42–56. doi:10.1016/j.compositesb.2018.04.027.

[3] Xiang D, Wang L, Tang Y, Zhao C, Harkin-Jones E, Li Y. Effect of phase transitions on the electrical properties of polymer/carbon nanotube and polymer/graphene nanoplatelet composites with different conductive network structures. Polym Int 2018;67:227–235. doi:10.1002/pi.5502.

[4] Kozioł M, Toroń B, Szperlich P, Jesionek M. Fabrication of a piezoelectric strain sensor based on SbSI nanowires as a structural element of a FRP laminate. Compos Part B Eng 2019;157:58–65. doi:10.1016/j.compositesb.2018.08.105.

[5] Liu X, Tang T-C, Tham E, Yuk H, Lin S, Lu TK, et al. Stretchable living materials and devices with hydrogel–elastomer hybrids hosting programmed cells. Proc Natl Acad Sci 2017;114:2200–2205. doi:10.1073/pnas.1618307114.

[6] Li Y, Samad YA, Taha T, Cai G, Fu SY, Liao K. Highly Flexible Strain Sensor from Tissue Paper for Wearable Electronics. ACS Sustain Chem Eng 2016;4:4288–4295. doi:10.1021/acssuschemeng.6b00783.

[7] Wang N, Xu Z, Zhan P, Dai K, Zheng G, Liu C, et al. A tunable strain sensor based on a carbon nanotubes/electrospun polyamide 6 conductive nanofibrous network embedded into poly(vinyl alcohol) with self-diagnosis capabilities. J Mater Chem C 2017;5:4408–4418. doi:10.1039/c7tc01123g.

[8] Vlăsceanu GM, Iovu H, Ioniţă M. Graphene inks for the 3D printing of cell culture scaffolds and related molecular arrays. Compos Part B Eng 2019;162:712–723. doi:10.1016/j.compositesb.2019.01.010.

[9] Wang H, Dai JG. Strain transfer analysis of fiber Bragg grating sensor assembled composite structures subjected to thermal loading. Compos Part B Eng 2019;162:303–313. doi:10.1016/j.compositesb.2018.11.013.

[10] Min SH, Lee GY, Ahn SH. Direct printing of highly sensitive, stretchable, and durable strain sensor based on silver nanoparticles/multi-walled carbon nanotubes composites. Compos Part B Eng 2019;161:395–401. doi:10.1016/j.compositesb.2018.12.107.

[11] Espera AH, Dizon JRC, Chen Q, Advincula RC. 3D-printing and advanced manufacturing for electronics. Prog Addit Manuf 2019;4:1-23. doi:10.1007/s40964-019-00077-7.

[12] Zhang Q, Zhang F, Xu X, Zhou C, Lin D. Three-Dimensional Printing Hollow Polymer Template-Mediated Graphene Lattices with Tailorable Architectures and Multifunctional Properties. ACS Nano 2018;12:1096–1106. doi:10.1021/acsnano.7b06095.

[13] Wei H, Li K, Liu WG, Meng H, Zhang PX, Yan CY. 3D Printing of Free-Standing Stretchable Electrodes with Tunable Structure and Stretchability. Adv Eng Mater 2017;19:1–6. doi:10.1002/adem.201700341.

[14] Christ JF, Aliheidari N, Ameli A, Pötschke P. 3D printed highly elastic strain sensors of multiwalled carbon nanotube/thermoplastic polyurethane nanocomposites. Mater Des 2017;131:394–401. doi:10.1016/j.matdes.2017.06.011.

[15] Kim K, Park J, Suh J hoon, Kim M, Jeong Y, Park I. 3D printing of multiaxial force sensors using carbon nanotube (CNT)/thermoplastic polyurethane (TPU) filaments. Sensors Actuators, A Phys 2017;263:493–500. doi:10.1016/j.sna.2017.07.020.

[16] Madni I, Hwang CY, Park SD, Choa YH, Kim HT. Mixed surfactant system for stable suspension of multiwalled carbon nanotubes. Colloids Surfaces A Physicochem Eng Asp 2010;358:101–107. doi:10.1016/j.colsurfa.2010.01.030.

[17] Legeza Ö, Roder J, Hess BAB a., Röder J. QC-DMRG study of the ionic-neutral curve crossing of LiF. Mol Phys 2009;101:2019-2028. doi:10.1080/002689703.

[18] Xiang D, Wang L, Zhang Q, Chen B, Li Y, Harkin-Jones E. Comparative study on the deformation behavior, structural evolution, and properties of biaxially stretched high-density polyethylene/carbon nanofiller (carbon nanotubes, graphene nanoplatelets, and carbon black) composites. Polym Compos 2018;39:E909–923. doi:10.1002/pc.24328.

[19] Pandele AM, Andronescu C, Vasile E, Radu IC, Stanescu P, Iovu H. Non-covalent functionalization of GO for improved mechanical performances of pectin composite films. Compos Part A Appl Sci Manuf 2017;103:188–195. doi:10.1016/j.compositesa.2017.10.005.

[20] Chen Q, Xiang D, Wang L, Tang Y, Harkin-Jones E, Zhao C, et al. Facile fabrication and performance of robust polymer/carbon nanotube coated spandex fibers for strain sensing. Compos Part A Appl Sci Manuf 2018;112:186–196.

doi:10.1016/j.compositesa.2018.06.009.

[21] Kim HJ, Sim K, Thukral A, Yu C. Rubbery electronics and sensors from intrinsically stretchable elastomeric composites of semiconductors and conductors. Sci Adv 2017;3:1–9. doi:10.1126/sciadv.1701114.

[22] Jeon JY, Ha TJ. Waterproof Electronic-Bandage with Tunable Sensitivity for Wearable Strain Sensors. ACS Appl Mater Interfaces 2016;8:2866–2871. doi:10.1021/acsami.5b12201.

[23] Hu C, Li Z, Wang Y, Gao J, Dai K, Zheng G, et al. Comparative assessment of the strain-sensing behaviors of polylactic acid nanocomposites: reduced graphene oxide or carbon nanotubes. J Mater Chem C 2017;5:2318–2328. doi:10.1039/c6tc05261d.

[24] Lin L, Liu S, Zhang Q, Li X, Ji M, Deng H, et al. Towards tunable sensitivity of electrical property to strain for conductive polymer composites based on thermoplastic elastomer. ACS Appl Mater Interfaces 2013;5:5815–5824. doi:10.1021/am401402x.

[25] Jeon H, Hong SK, Kim MS, Cho SJ, Lim G. Omni-Purpose Stretchable Strain Sensor Based on a Highly Dense Nanocracking Structure for Whole-Body Motion Monitoring. ACS Appl. Mater. Interfaces 2017;9,48:41712-41721. doi:10.1021/acsami.7b14153.

[26] Chen S, Wei Y, Wei S, Lin Y, Liu L. Ultrasensitive Cracking-Assisted Strain Sensors Based on Silver Nanowires/Graphene Hybrid Particles. ACS Appl Mater Interfaces 2016;8:25563–25570. doi:10.1021/acsami.6.

[27] Darabi MA, Khosrozadeh A, Mbeleck R, Liu Y, Chang Q, Jiang J, et al. Correction to: Skin-Inspired Multifunctional Autonomic-Intrinsic Conductive Self-Healing Hydrogels with Pressure Sensitivity, Stretchability, and 3D Printability. Adv Mater 2018;30:8–19. doi:10.1002/adma.201705922.

[28] Ryu S, Lee P, Chou JB, Xu R, Zhao R, Hart AJ, et al. Extremely Elastic Wearable Carbon Nanotube Fiber Strain Sensor for Monitoring of Human Motion. ACS Nano 2015;9:5929–5936. doi:10.1021/acsnano.5b00599.

[29] Cravanzola S, Haznedar G, Scarano D, Zecchina A, Cesano F. Carbon-based piezoresistive polymer composites: Structure and electrical properties. Carbon N Y 2013;62:270–277. doi:10.1016/j.carbon.2013.05.064.

[30] Lozano-Pérez C, Cauich-Rodríguez J V., Avilés F. Influence of rigid segment and carbon nanotube concentration on the cyclic piezoresistive and hysteretic

behavior of multiwall carbon nanotube/segmented polyurethane composites. Compos Sci Technol 2016;128:25–32. doi:10.1016/j.compscitech.2016.03.010.

[31] Lachhab A, Robin E, Le Cam JB, Mortier F, Tirel Y, Canevet F. Thermomechanical analysis of polymeric foams subjected to cyclic loading: Anelasticity, self-heating and strain-induced crystallization. Polymer (Guildf) 2017;126:19–28. doi:10.1016/j.polymer.2017.08.010.

[32] Reulier M, Matadi Boumbimba R, Walsh Korb Z, Vaudemont R, Avérous L. Thermomechanical and cyclic behavior of biocomposites based on renewable thermoplastics from dimer fatty acids. J Appl Polym Sci 2017;134:1–13. doi:10.1002/app.44610.

[33] Boland CS, Khan U, Backes C, O'Neill A, McCauley J, Duane S, et al. Sensitive, high-strain, high-rate bodily motion sensors based on graphene-rubber composites. ACS Nano 2014;8:8819–8830. doi:10.1021/nn503454h.

[34] Jia Y, Chen Z, Yan W. A numerical study on carbon nanotube pullout to understand its bridging effect in carbon nanotube reinforced composites. Compos Part B Eng 2015;81:64–71. doi:10.1016/j.compositesb.2015.07.003.

[35] Lin L, Liu S, Zhang Q, Li X, Ji M, Deng H, et al. Towards tunable sensitivity of electrical property to strain for conductive polymer composites based on thermoplastic elastomer. ACS Appl Mater Interfaces 2013;5:5815–5824. doi:10.1021/am401402x.

[36] Christ JF, Aliheidari N, Pötschke P, Ameli A. Bidirectional and stretchable piezoresistive sensors enabled by multimaterial 3D printing of carbon nanotube/thermoplastic polyurethane nanocomposites. Polymers (Basel) 2018;11. doi:10.3390/polym11010011.